Authors' accepted manuscript

59th 3AF International Conference on Applied Aerodynamics
24 – 26 March 2025, Strasbourg - France

AERO2025-06-DUQUESNE

DYNAMICS AND LOSSES OF A SHORT LAMINAR SEPARATION BUBBLE

Pierre Duquesne [(1)], Emmanuel Jondeau [(1)] and Marlène Sanjosé[(2)]
[(1)] *Ecole Centrale de Lyon, CNRS, Universite Claude Bernard Lyon 1, INSA Lyon, LMFA, UMR5509, 69130, Ecully, France, Email: pierre.duquesne@ec-lyon.fr*
[(2)] *École de Technologie Supérieure, Montréal, Québec H3C 1K3, Canada.*

ABSTRACT

A laminar separation bubble induced by an adverse pressure gradient is characterized using velocity field from Particle Image Velocimetry. The analysis of the velocity field statistics and time series snapshots observations confirm a laminar flow separation, followed by an unsteady turbulent boundary layer reattachment. The transition is initiated by a Kelvin-Helmholtz instability. The transition and reattachment of the separation is also analysed using Proper Orthogonal Decomposition and a decomposition of losses based on the mean kinetic energy equation. The instability generates a vortex at the mean bubble edge when viscous effects are important and Reynolds stresses are low. The vortex is transported along the edge. As the bubble height increases, the cross Reynolds stress and the vortex size increase. Finally, the vortex become sufficiently strong to induce a counter rotating vortex at the wall inside the bubble and the separation bubble break down.

1. INTRODUCTION

A Laminar Separation Bubble (LSB) corresponds to the separation and reattachment of a laminar boundary layer. LSB can be induced by an adverse pressure gradient on a relatively flat plane (in opposition to a backward-facing step separation). This flow can lead to the transition to turbulence. The turbulent mixing introduces energy from the external flow into the boundary layer, which causes the flow to reattach to the wall and closes the bubble. LSB is a classic issue in laminar-turbulent transition and stability studies [1, 2]. In terms of applied aerodynamics, LSB may be encountered on miniature UAV and turbomachinery, for example, on turbine [3] and fan blades [4]. LSB significantly alter the flow around the profiles, increasing losses and deteriorating aerodynamic performance and inducing noise.

Depending on the influence on the pressure distribution, two types of LSB can be distinguished [5]. Short bubbles, which have only a local effect on the pressure distribution, and long bubbles, which have a global influence on the pressure distribution. In a short bubble, the most common case, a Kelvin-Helmholtz (KH) type instability causes the rolling-up of the shear layer, which leads to the transition to turbulence. Long bubbles are characterized by an absolute instability with the development of roll-ups in the recirculation zone [6].
In this article, a short LSB is studied using two-component Particle Image Velocimetry (PIV) measurements. After a brief presentation of the setup and measurement technique, the global flow is described. A Proper Orthogonal Decomposition (POD) analysis, including low order reconstruction and conditional averaging is then used to illustrates the vortex ejection. Finally, the analysis focuses on the different loss mechanisms induced by the separation bubble and the link with the vortex ejection mechanism.

2. EXPERIMENTAL SET-UP

Experiments were conducted in the wind tunnel of the Laboratoire de Thermofluide pour le transport (TFT) at the École de Technologie Supérieure (ÉTS) in Montreal.

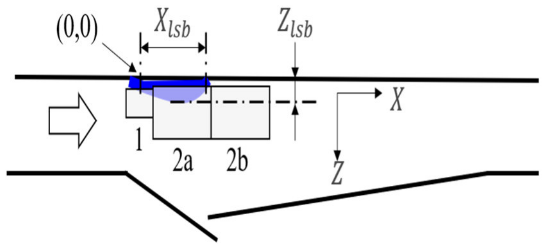

Figure 1. Wind tunnel sketch, PIV plane, measurement reference frame, and bubble position in blue.

The wind tunnel was specifically built to study separation bubbles induced by a pressure gradient [7]. It consists of three sections, the upstream section, which has a constant rectangular cross-section, allows the development of a two-dimensional laminar boundary layer over a length of approximately 1.5 m. The second section, shown in Fig. 1, allows for the imposition of the pressure gradient. The lower wall is inclined to form a diverging-converging channel. To ensure the boundary layer remains attached to the lower wall of the wind tunnel, a suction slot is installed on this wall. The boundary layer on the upper wall is subjected first to an adverse pressure gradient, then to a favorable pressure gradient. This induces separation and then reattachment of the boundary layer. Finally, the downstream section of the wind tunnel is a parallel channel opening to the atmosphere, with the same cross-section as the first section, allowing the turbulent boundary layer to reach an equilibrium state. The boundary layer studied is the one that develops along the upper wall. The vertical origin of the coordinate system, $Z = 0$, is placed at the lower wall. The e_z axis is oriented from the upper wall toward the lower wall. The axial origin of the coordinate system, $X = 0$, is located at the most upstream point where the mean axial velocity is measured to be zero. On figures, the separation bubble will be presented at the bottom, even though in the experiment it is located on the upper wall.

The upstream boundary layer is laminar, with a Reynolds number based on the momentum thickness of approximately Re_θ =400 [8].

The flow at separation is characterized by a velocity of U_∞ =3,7 m/s. The Mach number is approximately 0,01. The dimensions of the separation bubble, determined from PIV measurements, give a length of X_{lsb} = 194 mm and a height of Z_{lsb} =11,9 mm. By calculating a Reynolds number based on the height of the separation bubble $Re_h = U_\infty Z_{lsb}/\nu \approx 2800$ and a dimensionless number representing the velocity gradient (ΔU) across the separation bubble $\tilde{P} = \frac{{Z_{lsb}}^2}{\nu}\frac{\Delta U}{X_{lsb}}$ ≈-20, the bubble is classified as a short bubble according to the classification proposed by Diwan et al. [9].

The axial (U) and vertical (W) velocity components are measured at the center of the test section ($Y = 0$) using a PIV system. Fig. 1 shows the positions of the three measurement planes. The upstream plane (plane 1) covers the laminar portion of the bubble. Plane 2a is centered on the transition and reattachment zones of the bubble, while plane 2b, the most downstream, focuses on the boundary layer, which has become turbulent. Only measurement planes 2a and 2b are synchronized.

The PIV system consists of a pulsed Nd:YAG laser (EverGreen Quantel), delivering two laser pulses at a 532 nm wavelength and an energy of 400 mJ. The two pulses are separated by 500 µs to provide a balance between low- and high-speed regions in the flow. The laser beam is shaped into a sheet approximately 1 mm thick and oriented vertically to illuminate the center of the test section (see Fig. 2). Images are recorded at a frequency of 10 Hz using either one (plane 1) or two cameras (planes 2a and 2b) of type sCMOS (LaVision-16b) with a resolution of 2560 x 2160 pixels. For Plane 1, the camera is equipped with a 105 mm f/8 Nikon lens, while Planes 2a and 2b use a 50 mm f/8 Nikon lens. Images are calibrated using a LaVision 204-15 calibration target. A set of 1200 images is acquired for each measurement plane, corresponding to 2 minutes of measurement. The flow is seeded with droplets of Bis(2-ethylhexyl) sebacate less than 1 µm in diameter. Image processing is performed using LaVision DaVis software (version 8.4). The minimum image is subtracted from instantaneous images to reduce background noise. A multi-pass correlation algorithm with 50% overlap and a final interrogation window of 12 x 12 pixels is used. At each iteration, correlation validation is performed to remove vectors with ambiguous correlations (the main correlation peak must be at least 30% higher than secondary peaks). A post-validation check confirms the absence of peak locking. The vector fields are then linearly interpolated onto a uniform grid.

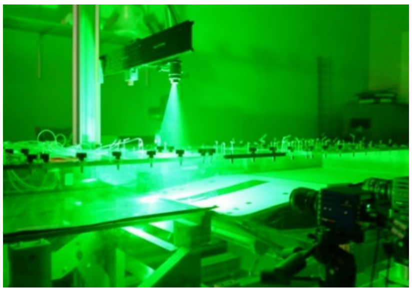

Figure 2. PIV setup

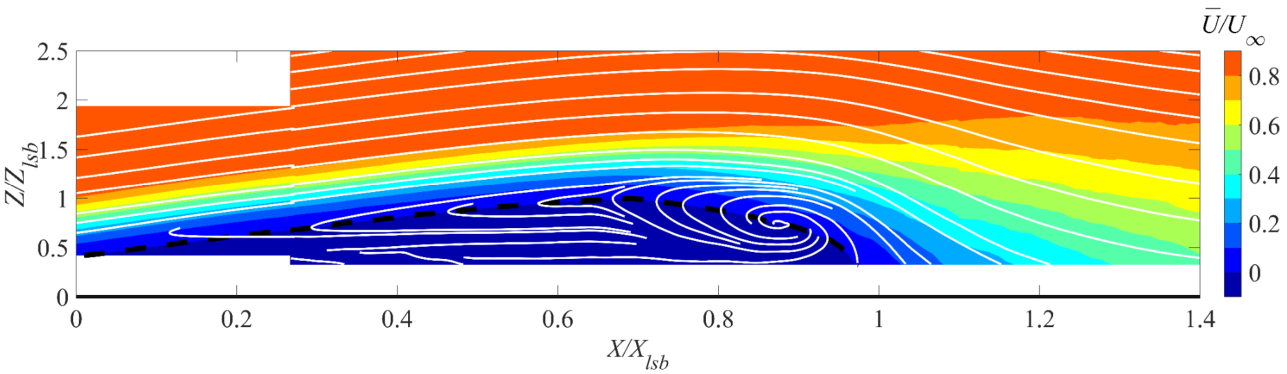

Figure 3. Mean axial velocity normalized by U_∞. The black dashed line represents zero mean axial velocity (bubble boundary). The streamlines are shown in white.

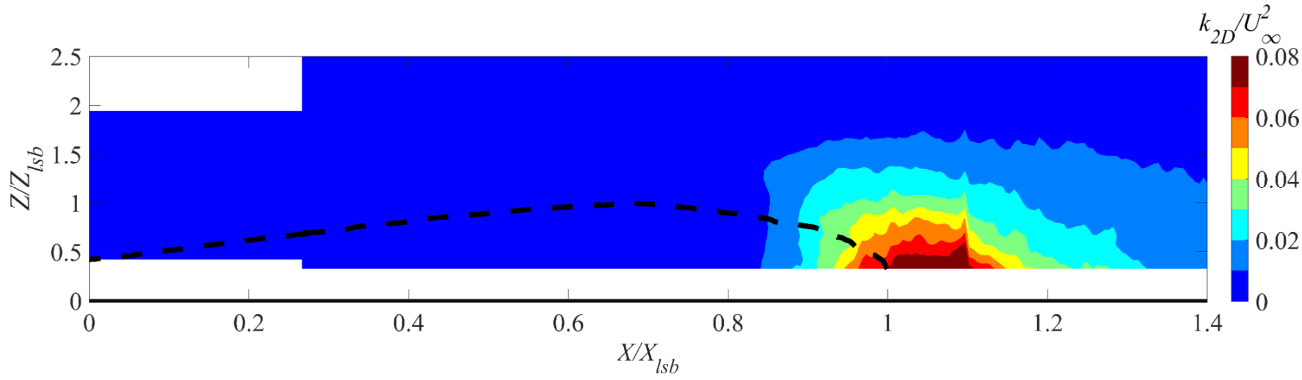

Figure 4. Partial turbulent kinetic energy. The black dashed line represents zero mean axial velocity (bubble boundary).

At the end, only the portion of the field containing the bubble is used for analysis. The selection for plane 1 covers approximately 100 x 18 mm (206 x 38 vectors), while the combined area of planes 2a and 2b is 334 x 28 mm (335 x 29 vectors). To facilitate interpretation, the figures in this article have a different aspect ratio from reality: the vertical dimension is doubled. Details on PIV processing including uncertainties estimation can be found in [10].

3. LSB DESCRIPTION

Fig. 3 shows the mean axial velocity field. The mean axial velocity equal to zero was chosen as an indicator of the separation bubble contours and is shown in black dash line on the various figures. The streamlines of the global flow are deflected by the presence of the separation bubble. The axial flow component within the bubble is opposite to that of the global flow, indicating the recirculation zone. The fluid inflow into the bubble can be observed through the wrapping of streamlines on the downstream side of the separation bubble.

The partial turbulent kinetic energy (k_{2D}) field is shown in Fig. 4. The partial turbulent kinetic energy includes only two of the three velocity components and is calculated using Equation (1).

$$k_{2D} = \frac{1}{2}\left(\overline{u'u'} + \overline{w'w'}\right) \tag{1}$$

It should be noted that the spatial resolution of the velocity measurements does not allow for quantification of fluctuations at the smallest turbulence scales. The upstream part of the flow exhibits a low level of turbulent kinetic energy, both in the global flow and within the bubble. This highlights a laminar regime and a stationary separation point. Downstream of the maximum thickness of the separation bubble, the turbulent kinetic energy increases, reaching its peak just after the mean reattachment point, emphasizing its unsteady nature. The separation bubble induces the transition to turbulent flow. This additional energy, which appears downstream of the separation bubble, contributes to the reattachment of the bubble by energizing the boundary layer. These observations are consistent with the instantaneous velocity fields, which are not presented here.

Fig. 5 shows the instantaneous vorticity field from planes 2a and 2b. This instant is representative of the observations made from the 120-second sequences recorded. In the most upstream part, the streamlines show the formation of a clockwise vortex centered around the contour of the separation bubble. Downstream of this first vortex, a second vortex is ejected from the bubble. This vortex has a more cylindrical shape and a higher vorticity at its center. Further downstream of this second vortex, numerous positive and negative vorticity spots are visible. These correspond to the breakdown of vortices induced by the KH instability into smaller vortices. After a calm zone between X/X_{lsb} =1.35 and X/X_{lsb} = 1.45, vorticity spots become visible again at the downstream end of the measurement plane. These likely originate from the breakdown of a previous vortex that has been convected further downstream by the flow. This instant is representative of the evolution of vortices generated in the shear layer induced by the bubble. This

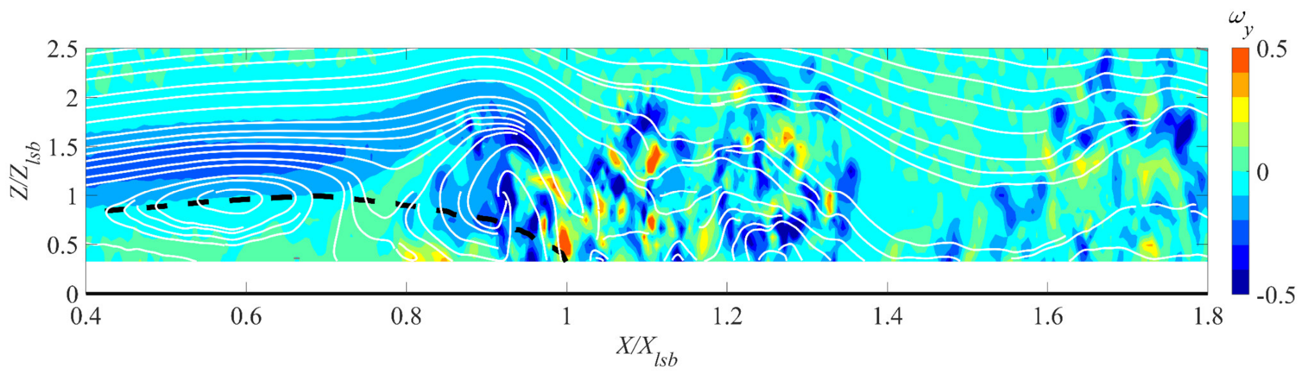

Figure 5. Instantaneous planar vorticity. The black dashed line represents zero mean axial velocity (bubble boundary). Streamlines calculated from the unsteady field are shown in white.

mechanism is consistent with a short LSB. Friction measurements on the same configuration show a phenomenon around 20-25 Hz, which can be associated with vortex shedding from the KH instability [8]. This frequency is too high to allow temporal tracking of the vortices with the PIV measurement system, which is not time-resolved.

4. POD ANALYSIS

A snapshot POD is used on the velocity fields [11]. The unsteady velocity vector field $\boldsymbol{u}(\boldsymbol{x},t)$ is decomposed into an infinite set of spatial orthogonal functions $\boldsymbol{\phi}^m(\boldsymbol{x})$ called POD modes. Here, the velocity vector field is used instead of the velocity fluctuation vector, $\boldsymbol{u}'(\boldsymbol{x},t)$. Note that both POD analyses were conducted and confirmed to the same conclusion. These POD modes have the largest mean square projection on the velocity field. In practice, the velocity field is approximated with a finite number of M modes by:

$$\boldsymbol{u}(\boldsymbol{x},t) = \sum_{m=1}^{+\infty} a^m(t)\boldsymbol{\phi}^m(\boldsymbol{x}) \approx \sum_{m=1}^{M} a^m(t)\boldsymbol{\phi}^m(\boldsymbol{x}) \qquad (2)$$

where $a^m(t)$ is the temporal coefficient that quantify the amplitude variation of each POD mode. Here, the problem is solved in a spatially and temporally discretised form on a two-dimensional spatial domain. The type of discrete datasets considered is M uncorrelated velocity field realisations (named snapshots) in a plane consisting of N data points, and two velocity components per point. The POD optimisation problem is equivalent to solving the following eigenvalue problem:

$$\boldsymbol{CA} = \lambda \boldsymbol{A} \qquad (3)$$

where $\boldsymbol{C} = 1/M\,(\boldsymbol{UU}^T + \boldsymbol{WW}^T)$ is the spatial correlation matrix, $\boldsymbol{U}$ and $\boldsymbol{W}$ are the matrices of each velocity component for all velocity field realisations ($M \times N$). Here the spatial correlation matrix is based on the kinetic energy with both velocity components to assure a coherence between mode in the two directions. The POD mode components $\phi_x^m(\boldsymbol{x})$ and $\phi_z^m(\boldsymbol{x})$ are obtained by projecting, respectively, $\boldsymbol{U}$ and $\boldsymbol{W}$ on the corresponding eigenvector $\boldsymbol{A}^m$:

$$\phi_x^m(\boldsymbol{x}) = \boldsymbol{U}^T\boldsymbol{A}^m; \phi_y^m(\boldsymbol{x}) = \boldsymbol{W}^T\boldsymbol{A}^m \qquad (4)$$

By convention, the POD modes are sorted in ascending order of kinetic energy. Here, the mode 1 is the mode with the highest level of the fluctuating kinetic energy. The zero mode represents the mean mode (with the highest level of the kinetic energy). The POD computation is performed with a MATLAB code (inspired by the one of [12]). In addition, an automated vortex detection method is used on the different fields (as describes in [13, 14]).

POD analysis has been conducted on plane 2 (a and b in same times). Fluctuating kinetic energy represents 5% of the total energy. That is coherent with a large part of the field of view with high velocity and few fluctuation and a small portion of low velocity and fluctuation (LSB and its vicinity). Fig. 6 shows the mode 1, representing 10% of the fluctuating kinetic energy. This mode is composed by a succession of rotating-contrarotating vortices. The first high-vorticity vortex is located just upstream of the point of maximum thickness of the mean bubble. Successive vortices increase in size and intensity up to the mean reattachment point. Downstream vortices become larger and larger but their vorticity decreases and the coherence of vortices is less evident. The position, intensity and direction of vortices can be different but the previous description is common to the first seventeen POD modes. These modes all together represent 58% of the fluctuating kinetic energy and can be associated to the vortex generation. The succession of rotating-contrarotating vortices in the first modes can be observed in other POD decomposition applied on an LSB, as for example in [14, 15]. Further mode in the decomposition associated with lower energy show more various patterns and appear less coherent.

To confirm this and explore the mechanism in the next section, reduce order model reconstruction using POD modes and conditional averaging is proposed. Fig. 7 presents an example of reconstruction of an unsteady field. The top Fig. 7A is the original field (from the measurement, i.e with all POD modes included), the middle Fig. 7B is a reconstruction with only the seventeen first fluctuating modes and Fig. 7C is the reconstruction

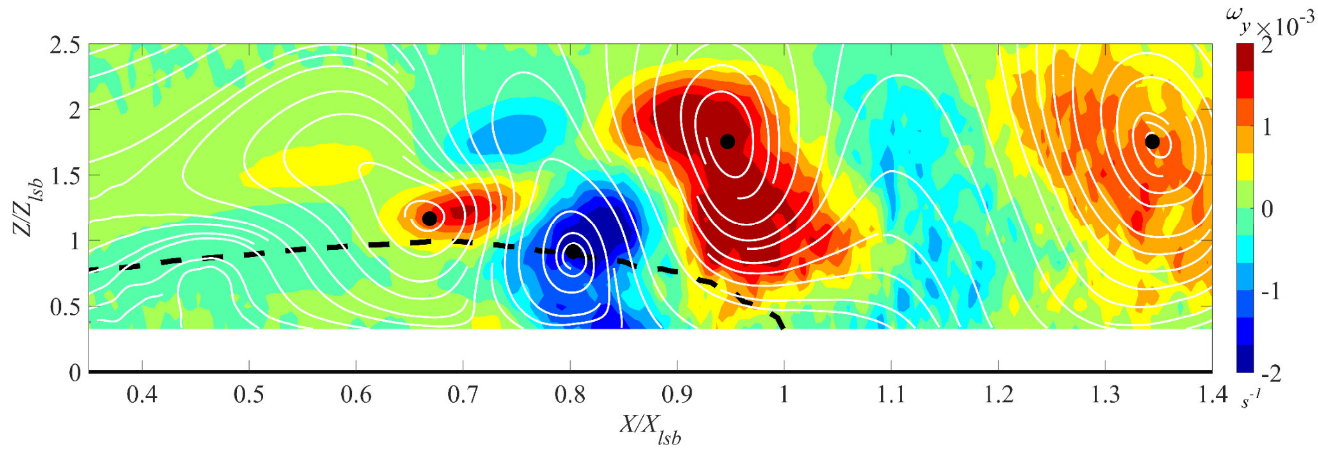

Figure 6: Planar vorticity field calculated on the first POD mode (ϕ_x^1, ϕ_z^1). The black dashed line, and dots represent respectively, the bubble boundary and vortex centers. The streamlines calculated on the first POD mode are shown in white.

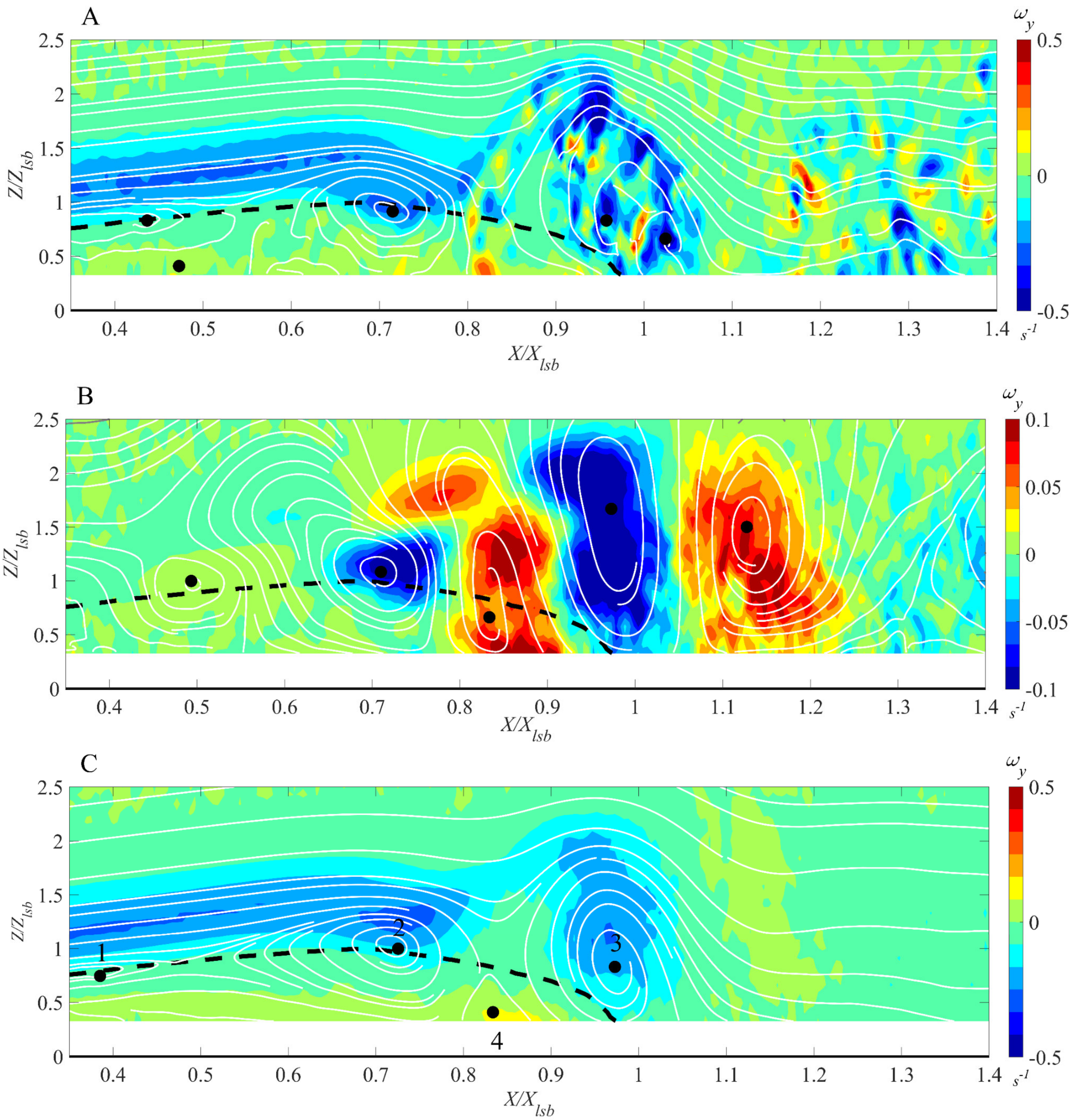

Figure 7: Planar vorticity field calculated on A) unsteady velocity field, B) the reconstruction with the seventeen first fluctuating POD modes, C) the reconstruction with the zero POD mode (i.e. the average) and the seventeen first fluctuating POD modes. The black dashed line, and dots represent respectively, the bubble boundary and vortex centers. The streamlines calculated on the different reconstructions are shown in white.

including mode 0 (the average) and the seventeen first fluctuating modes. The reconstruction with the seventeen first fluctuating modes (Fig. 7B) is consistent with the description of individual POD mode: a succession of rotating-contrarotating vortices. The superposition of these modes modulated by their respective temporal coefficient allow to represent the evolution of the vortices ejection at different instant. In the reconstruction including the average field (presented Fig. 3), at bubble outside and at the border only clockwise vortices can be observed. The most upstream vortex (1 in Fig. 7C) is at the mean bubble boundary. It is small, elongated in the axial direction and with low level of vorticity. Further downstream another vortex (2 in Fig. 7C) is also at the mean bubble boundary. This second vortex is larger (same order of magnitude of the LSB height), has a more cylindrical shape and higher vorticity (keep in mind that the vertical dimension is doubled in figures, so real vortex are more elongated in axial direction that the vortex representation). The furthest downstream vortex (3 in Fig. 7C) has the same level of vorticity, a cylindrical shape and larger but still with a size similar to the LSB height. This vortex is not on the mean bubble boundary. These different clockwise vortices correspond to different stage of the vortex ejection process. Fig. 7C highlights the thin vorticity layers (or braids) that interconnects the successive clockwise vortices (labeled 1, 2, and 3 in Fig. 7C), as suggested by [17]. In fig 7C, an anticlockwise vortex inside the LSB near the wall is visible (4 in Fig. 7C). To the best of the authors' knowledge, this is the first documentation of this vortex in an LSB. Previous studies on vortex formation and breakup in LSBs, such as [15, 18, 19], present mechanisms that do not include this one.

This instant has been selected because of its completeness. All snapshots have been reconstructed and analyzed, thanks to automatized vortex detection, the most upstream vortex (1 in Fig. 7C) is present in 25% of cases. Depending on the stage in the vortex ejection process, this vortex is being formed or already presents at slightly different locations. The anticlockwise vortex inside the bubble (4 in Fig. 7C) is present in 14% of snapshots. It is at the limit of the PIV field. It might be present more often than observed due to the limited access to the wall vicinity in the PIV fields. This one is probably too small and/or too close to the wall to be captured with the present setup. Its existence is also supported by a zone of positive vorticity near the wall. Comparison between the original field and the reconstructions confirm that the family of fluctuating modes is representative of the vortex ejection process.

A drawback of the POD analysis is the actual representativity of the mathematical modes. To confirm the vortex ejection process, a conditional averaging based on the dominant fluctuating POD mode has been used. Each original unsteady velocity field (without POD reconstruction) is sorted based on the maximum absolute value of the temporal coefficient $a^m(t)$ of its POD decomposition. The temporal coefficient can be positive or negative, distinguishing different contributions to the fluctuating velocity fields. Original velocity fields with the same dominant mode and the same sign are averaged together. Ninety percent of all POD-fields have a maximal absolute value of the temporal coefficient in the five first fluctuating modes. The last 10% are distributed in the other fluctuating modes limiting the statistical significance. For this reason, only the conditional averaging with the first five modes are analyzed. These

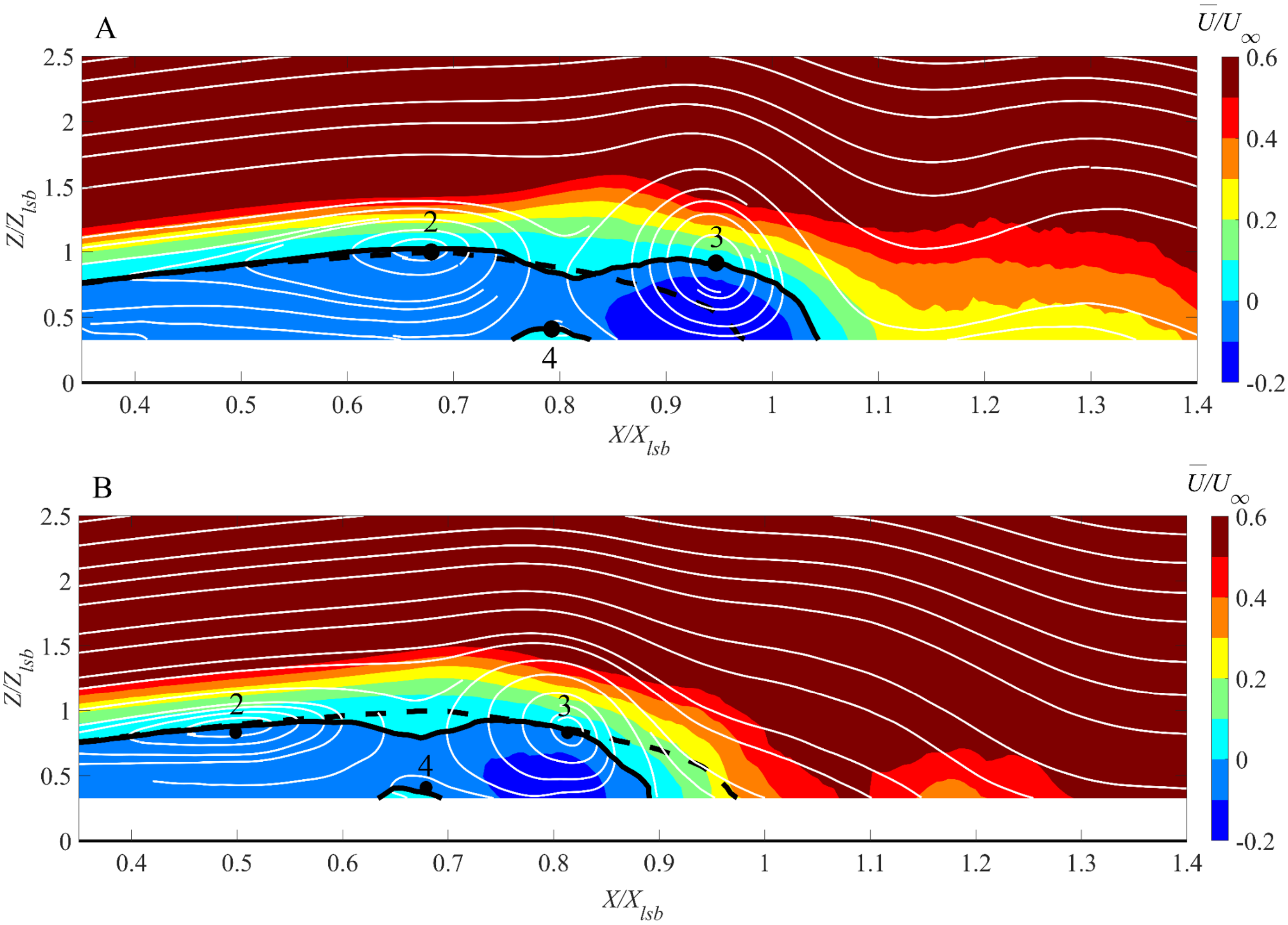

Figure 8: Axial velocity of the conditional averaging with the first POD mode. The upper view (lower view) corresponds to high positive (negative) mode amplitude. The black solid line, dashed line, and dots represent, respectively, the average filtered axial velocity equal to 0, the bubble boundary and vortex centers. The streamlines calculated on the different averaged field are shown in white.

five modes represent 42% of the fluctuating energy. In Fig. 8, the conditional-average of the axial velocity and some streamlines for the first fluctuating POD mode are shown. The upper view corresponds to positive temporal coefficients value and the lower view corresponds to negative value. The vortex ejection description for both fields is aligned with the one with the POD reconstruction based on the first 17 modes. An elongated clockwise vortex (noted 2 in Fig. 8) is present at the mean bubble boundary (dash line in Fig. 8). A second clockwise vortex (noted 3 in Fig. 8) is downstream with a more cylindrical shape. This vortex is not along the mean bubble boundary, but on the conditional averaged bubble boundary (solid line in Fig. 8). Finally, the existence of the anticlockwise vortex (noted 4 in Fig. 8) is confirmed inside the LSB near the wall. This description is similar to other conditional averaging field. In some cases, an additional clockwise vortex at the more upstream can be visible (as vortex 1 in Fig 7) and the anticlockwise vortex can be absent. As can be observed in Fig. 8A and 8B, the downstream position of conditional averaged bubble boundary differs a lot between the different dominant POD modes. This observation made here between negative and positive value of a same mode can be extended between the different modes. This confirms that the different POD modes are representative of the different stage of the vortex ejection process.

5. LOSSES ANALYSIS

Using the Reynold decomposition between the average $\overline{U}(x)$ and the fluctuation $u'(x,t)$, the mean kinetic energy equation using the Einstein decomposition for an incompressible flow is,

$$\overline{U}_j \frac{\partial \frac{1}{2}\overline{U}_i\overline{U}_i}{\partial x_j} = \frac{\partial}{\partial x_j}\left(-\frac{P}{\rho}\overline{U}_j + 2\nu\overline{U}_i S_{ij} - \overline{u'_i u'_j}\,\overline{U}_i\right) - 2\nu S_{ij}S_{ij} + \overline{u'_i u'_j}\,S_{ij} \quad (5)$$

with S_{ij} the mean strain rate tensor. This equation can be rewrite as [10, 17]:

$$-\overline{U}_j\frac{\partial}{\partial x_j}\left(\frac{1}{2}\rho\overline{U}_i\overline{U}_i + P\right) = \underbrace{\mu\left(\frac{\partial\overline{U}_i}{\partial x_j}\right)^2}_{\mathrm{I}} \underbrace{-\rho\overline{u'_i u'_j}\frac{\partial\overline{U}_i}{\partial x_j}}_{\mathrm{II}} \underbrace{-\mu\frac{\partial}{\partial x_j}\left(\overline{U}_i\frac{\partial\overline{U}_i}{\partial x_j}\right)}_{\mathrm{III}} + \underbrace{\frac{\partial\,\overline{U}_i\left(\rho\overline{u'_i u'_j}\right)}{\partial x_j}}_{\mathrm{III}} \quad (6)$$

For a steady and homogeneous flow, the left-hand term corresponds to the material derivative of the total pressure. The negative sign in front of equation (6) associates a decrease in total pressure with losses (positive in sign). Term I represents the generation of losses due to viscous effects. Term II represents the variation of losses related to energy transfer between the mean flow and fluctuations. This term also corresponds to the production of turbulent kinetic energy multiplied by the density. Terms III and IV represent transport terms, respectively by viscous stresses and velocity fluctuations. These terms can be projected onto different axes; Table 1 presents the components of each term that are accessible through measurements of the two velocity components. Dominant terms are highlighted in green in Table 1.

Table 1: Terms of equation 6 accessible through measurements. Green terms are dominant.

(6)	Terms accessible through 2C-PIV measurements
I	$\mu(\partial\overline{U}/\partial x)^2, \mu(\partial\overline{U}/\partial z)^2,$ $\mu(\partial\overline{W}/\partial x)^2, \mu(\partial\overline{W}/\partial z)^2$
II	$-\rho\overline{u'u'}(\partial\overline{U}/\partial x), -\rho\overline{u'w'}(\partial\overline{U}/\partial z),$ $-\rho\overline{u'w'}(\partial\overline{W}/\partial x), -\rho\overline{w'w'}(\partial\overline{W}/\partial z)$
III	$-\mu\frac{\partial}{\partial x}(\overline{U}\,\partial\overline{U}/\partial x), -\mu\frac{\partial}{\partial z}(\overline{U}\,\partial\overline{U}/\partial z),$ $-\mu\frac{\partial}{\partial x}(\overline{W}\ \partial\overline{W}/\partial x), -\mu\frac{\partial}{\partial z}(\overline{W}\ \partial\overline{W}/\partial z)$
IV	$\rho(\partial\overline{U}(\overline{u'u'})/\partial x), \rho(\partial\overline{U}(\overline{u'w'})/\partial z),$ $\rho(\partial\overline{W}(\overline{u'w'})/\partial x), \rho(\partial\overline{W}(\overline{w'w'})/\partial z)$

Among the terms contributing to loss generation due to viscous effects, the only significant contribution is $\mu(\partial\overline{U}/\partial z)^2$. As shown in Fig. 9, these losses are located in the high-shear region just above the laminar part of the bubble. This region is also the braids zone. The term $\mu(\partial\overline{W}/\partial x)^2$ is negligible, indicating that the shear is dominated by the vertical variation of the axial velocity. At a X/X_{lsb} position, the maximum shear (and so viscous losses) are approximately located at the height corresponding to the mid-range of the axial velocity. The KH instability is well-modeled by linear stability theory [21], where viscosity does not play a determining role in the instability. However, the superposition of regions with high viscous losses and braids suggests that viscosity influences the vortex decomposition mechanism. The unsteady roll-ups induced by KH instability mix regions of low and high velocity, reducing the velocity gradient and, consequently, the viscous losses downstream of the bubble. When the viscous effect becomes too weak, the vorticity link (braids) between successive vortices is lost. The only significant viscous transport term is $-\mu\frac{\partial}{\partial z}(\overline{U}\,\partial\overline{U}/\partial z)$ and represents the transport of viscous forces by axial velocity. This term is important above and below the zone of high viscous loss generation. Fig. 9 also shows position of upstream vortices centers extracted from the different conditional averaging (noted 2 in Fig. 8 for example). These vortices, presented Fig. 9, are located at the mean bubble boundary above the high-shear region. These vortices seem too small to induce a significant turbulent production (as can be noticed in figure 10A).

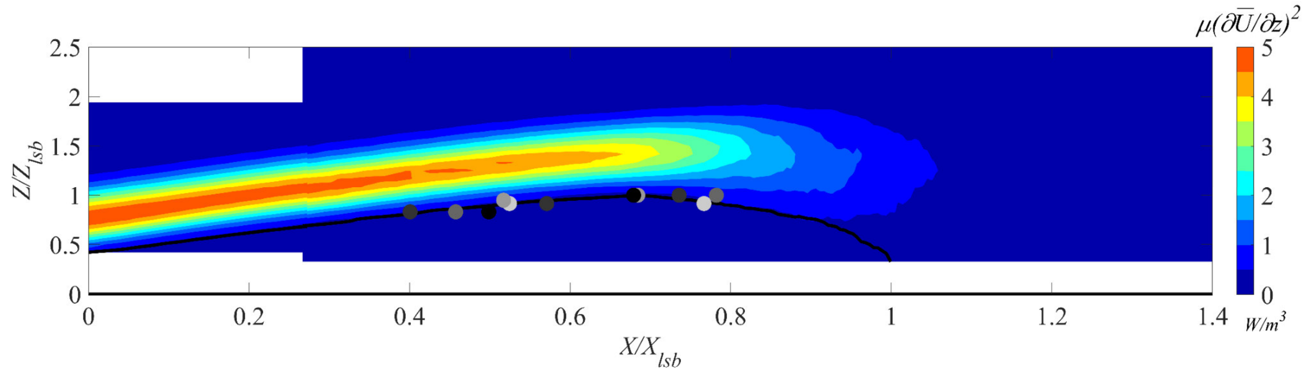

Figure 9: Viscous term $\mu(\partial U/\partial z)^2$. The black dashed line and dots represent, respectively, the bubble boundary and upstream vortex centers for the different conditional averaging (noted 1 in Fig. 8 for example). Dots color is from black to white, from the first to fifth POD modes.

The term of turbulent production $-\rho\overline{u'w'}(\partial\bar{U}/\partial z)$ is dominant and corresponds to the mechanism generating the most losses in the flow. This term becomes significant when the cross Reynolds stress $(\overline{u'w'})$ and/or the velocity gradient $\partial\bar{U}/\partial z$ are large. As shown in Fig. 10 A, this corresponds to the region of vortex ejections. In this region, large vortices induce significant axial and vertical velocity fluctuations, and the velocity deficit caused by the separation bubble creates a velocity gradient. Upstream of this region, the velocity gradient is larger (as can be noticed with the high level of the viscous term Fig. 9) but the cross Reynolds stress is weak. While downstream, the mean axial velocity deficit rapidly decreases, inducing a reduction of the turbulent production. The turbulent transport term $\rho\left(\partial\bar{U}(\overline{u'w'})/\partial z\right)$, (not shown here) is dominant among the turbulent transport terms and corresponds to the transport of cross fluctuations by the axial flow. This transport is important in the zone of high turbulent production. Fig. 10A also shows position of downstream vortices centers extracted from the different conditional averaging (noted 3 in Fig. 8 for example). These vortices are located above the high turbulent production $-\rho\overline{u'w'}(\partial\bar{U}/\partial z)$ region and can be visible or absent along the mean bubble boundary. This clearly highlights that large downstream vortices contribute significantly to velocity fluctuations in particular the $\overline{u'w'}$.

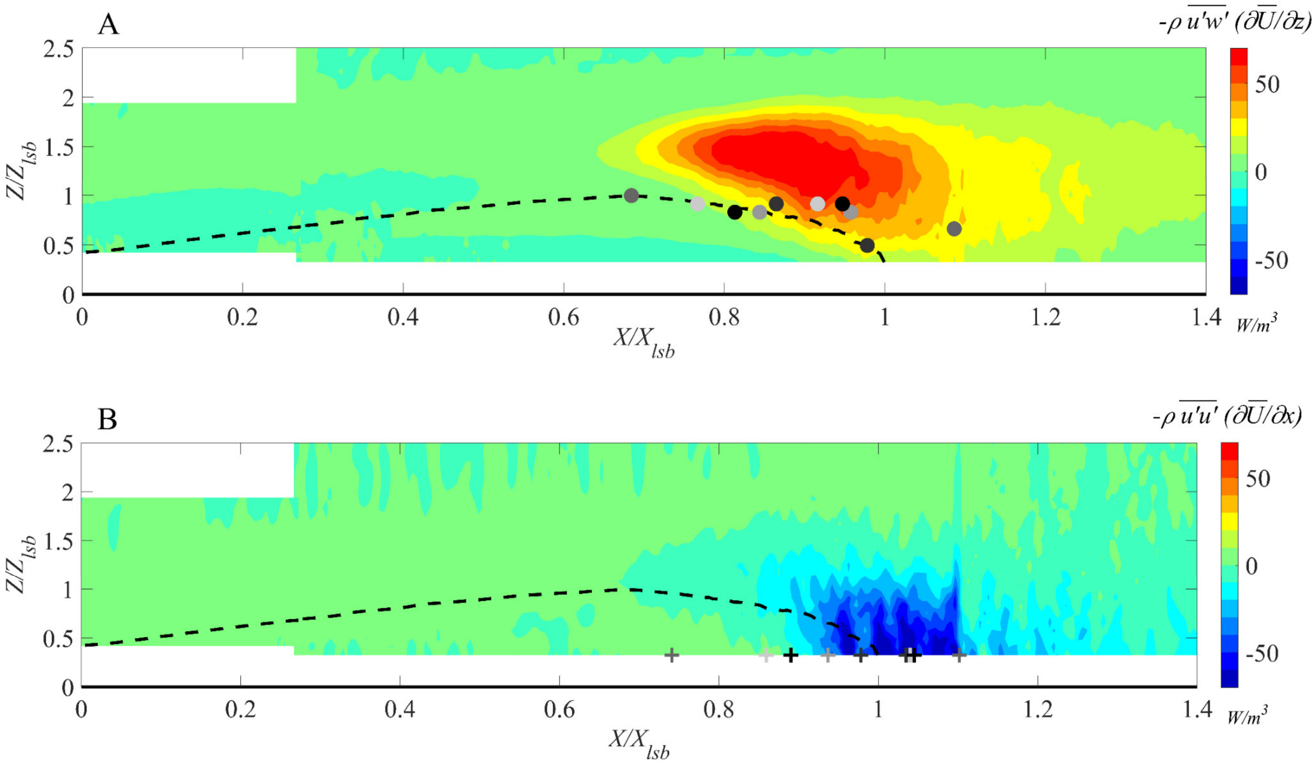

Figure 10: Turbulent production term, $-\rho\overline{u'w'}(\partial\bar{U}/\partial z)$ (A) and $-\rho\overline{u'u'}(\partial\bar{U}/\partial x)$ (B). The black dashed line represents the bubble boundary. Crosses and dots represent, respectively, the downstream limit of the bubble and the downstream vortex centers (noted 3 in Fig. 8 for example) for the different conditional averaging. Crosses and Dots color is from black to white, from the first to fifth POD modes.

As shown in Fig. 10B, the turbulent production term $-\rho\overline{u'u'}(\partial\overline{U}/\partial x)$ is negative around the reattachment point of the mean flow. The other measured turbulent production terms are not negative. A part of the energy is transferred between fluctuation components. The summation of all measured term is negative, which can be interpreted as an energy transfer from the fluctuations to the mean flow even if some component is not measured. This region corresponds to the energization of the boundary layer, contributing to its reattachment. Fig. 10B also shows position of downstream limit of the bubble from the different conditional averaging. These variation of the position of the bubble are well superposed with the zone of high turbulent production term. This confirms the link between boundary layer energization and its reattachment. Downstream of the bubble, a region with slightly negative turbulent production $-\rho\overline{u'u'}(\partial\overline{U}/\partial x)$ is also present. The axial velocity fluctuations contribute to downstream convection of the mean flow in the bubble's wake. The other turbulent production terms in the wake compensate for the term $-\rho\overline{u'u'}(\partial\overline{U}/\partial x)$, indicating an energy transfer in this region of the global flow to the fluctuations.

Combining the POD and losses analysis, the dynamics of the vortex ejection mechanism are proposed as follows. The initial vortex develops at the bubble boundary in the laminar region (1 in Fig. 7) through the amplification of the inviscid KH instability. The vortex is then convected downstream by the external flow growing, particularly in the axial direction. In the vertical direction, vortex expansion is restricted by the bottom wall and the high-velocity region above the LSB. As the bubble height increases, the influence of the wall decreases, allowing the vortex to expand vertically as well. The redistribution of velocity from the axial to the vertical component reduces the vertical gradient of axial velocity, leading to a significant reduction in viscous effects while simultaneously increasing the influence of the cross Reynolds stress. In the downstream part of the bubble, two successive clockwise vortices (2 and 3 in Fig. 7) interact with the wall shear layer, inducing a counter-rotating vortex near the wall inside the bubble. Vortex ejection corresponds to the combined effects of the positive axial velocity induced by the counter-rotating vortex at the wall and the vorticity layer breakup at the upper part of the LSB, caused by the velocity gradient reduction. The counter-rotating vortex is not documented in existing LSB literature and may represent a unique case for this particular LSB. Furthermore, the counter-rotating vortex is not observed during every ejection event (partly due to experimental limitations), suggesting that the described mechanism may coexist with a two-clockwise-vortices ejection mechanism in certain scenarios. Bubble break down leads to the mixing of high- and low-energy regions, which energizes the boundary layer and prevents subsequent separation. Finally, the vortex in the bubble wake breaks down into smaller vortices.

6. CONCLUSION

In this paper, a short laminar separation bubble induced by an adverse pressure gradient is characterized using velocity fields obtained from two-component Particle Image Velocimetry. Statistical analysis of the measurements reveals a classical averaged separation bubble structure, including a recirculation zone and the wrapping of streamlines on the downstream side of the separation bubble. The upstream portion of the flow exhibits a low level of turbulent kinetic energy, corresponding to a laminar regime and a stationary separation point. Fluctuations reach their peak just after the mean reattachment point, highlighting the unsteady nature of the reattachment. The instantaneous vorticity field reveals successive vortices induced by a Kelvin-Helmholtz (KH) instability.

Based on Proper Orthogonal Decomposition (POD) analysis, different vortices are identified. First, a succession of clockwise vortices is observed, corresponding to various stages of vortex dynamics: initiation in the laminar region, extension along the mean bubble boundary, and ejection. These vortices are connected by a thin vorticity layer until the complete detachment of the vortex from the LSB. Additionally, in some cases an anticlockwise vortex is observed for the first time and may play a role in the vortex ejection process.

Loss analysis is performed based on the mean kinetic energy equation. Results highlight the role of viscosity in the vorticity linkage between successive vortices. The redistribution of velocity from the axial to the vertical component reduces the vertical gradient of axial velocity, significantly decreasing viscous effects while simultaneously increasing the influence of the cross Reynolds stress. Moreover, some turbulent terms related to energy losses present negative values, which are interpreted as the energization of the boundary layer, contributing to its reattachment.

Finally, based on all these analyses, an ejection process is proposed.

Acknowledgments

The authors would like to express their gratitude to the prof Stephane Moreau, Université de Sherbrooke, for providing the PIV instrumentation. This project was made possible through the France-Québec Samuel-De Champlain cooperation program and the support of the Consortium for Industry-University Research in Turbomachinery (CIRT).

7. REFERENCES

[1] A. V. Dovgal, V. V. Kozlov, et A. Michalke, « Laminar boundary layer separation: Instability and associated phenomena », *Prog. Aerosp. Sci.*, vol. 30, nº 1, p. 61-94, janv. 1994, doi: 10.1016/0376-0421(94)90003-5.

[2] D. Rodríguez, E. M. Gennaro, et L. F. Souza, « Self-excited primary and secondary instability of laminar separation bubbles », *J. Fluid Mech.*, vol. 906, p. A13, janv. 2021, doi: 10.1017/jfm.2020.767.

[3] R. E. Mayle, « The Role of Laminar-Turbulent Transition in Gas Turbine Engines », présenté à ASME 1991 International Gas Turbine and Aeroengine Congress and Exposition, American Society of Mechanical Engineers Digital Collection, mars 2015. doi: 10.1115/91-GT-261.

[4] J. Al-Am, V. Clair, A. Giauque, J. Boudet, et F. Gea-Aguilera, « On the effects of a separation bubble on fan noise », *J. Sound Vib.*, vol. 537, oct. 2022, doi: 10.1016/j.jsv.2022.117180.

[5] P. R. Owen et L. Klanfer, « On the laminar boundary layer separation from the leading edge of a thin aerofoil », 1955.

[6] M. Dellacasagrande, D. Lengani, D. Simoni, et S. Yarusevych, « A data-driven analysis of short and long laminar separation bubbles », *J. Fluid Mech.*, vol. 976, p. R3, déc. 2023, doi: 10.1017/jfm.2023.960.

[7] A. M. Taifour, Q. Schwaab, J. Pioton, et J. Weiss, « A new wind tunnel for the study of pressure-induced separating and reattaching flows », *Aeronaut. J. -New Ser.-*, vol. 119, p. 91-108, janv. 2015, doi: 10.1017/S0001924000010265.

[8] A. M. Taifour, M. Sanjosé, et J. Weiss, « Unsteadiness in a Pressure-Induced Laminar Separation Bubble », Engineering, Turbulence, Modelling and Measurements (ETMM13), Rhodes, Greece, sept. 2021.

[9] S. S. Diwan, S. J. Chetan, et O. N. Ramesh, « On the bursting criterion for laminar separation bubbles », in *IUTAM Symposium on Laminar-Turbulent Transition*, R. Govindarajan, Springer, 2006, p. 401-407. doi: 10.1007/1-4020-4159-4_57.

[10] P. Duquesne, E. Jondeau, et M. Sanjose, « Investigation des mécanismes de pertes dans une bulle de décollement laminaire en PIV », Congrès Francophone de Techniques Laser, Lyon, sept. 2024.

[11] L. Sirovich, « Turbulence and the dynamics of coherent structures part i: coherent structures », *Appl. Math*, vol. 45, 1987.

[12] J. Weiss, « A Tutorial on the Proper Orthogonal Decomposition », in *AIAA Aviation 2019 Forum*, in AIAA AVIATION Forum. , American Institute of Aeronautics and Astronautics, 2019. doi: 10.2514/6.2019-3333.

[13] S. Depardon, J. J. Lasserre, L. E. Brizzi, et J. Borée, « Instantaneous skin-friction pattern analysis using automated critical point detection on near-wall PIV data », *Meas. Sci. Technol.*, vol. 17, nº 7, p. 1659, juill. 2006, doi: 10.1088/0957-0233/17/7/004.

[14] S. Depardon, J. J. Lasserre, L. E. Brizzi, et J. Borée, « Automated topology classification method for instantaneous velocity fields », *Exp. Fluids*, vol. 42, nº 5, p. 697-710, mai 2007, doi: 10.1007/s00348-007-0277-3.

[15] J. W. Kurelek, S. Yarusevych, et M. Kotsonis, « Vortex merging in a laminar separation bubble under natural and forced conditions », *Phys. Rev. Fluids*, vol. 4, nº 6, p. 063903, juin 2019, doi: 10.1103/PhysRevFluids.4.063903.

[16] D. Lengani, D. Simoni, M. Ubaldi, P. Zunino, et F. Bertini, « Analysis of the Reynolds stress component production in a laminar separation bubble », *Int. J. Heat Fluid Flow*, vol. 64, p. 112-119, avr. 2017, doi: 10.1016/j.ijheatfluidflow.2017.03.001.

[17] C. M. Ho et P. Huerre, « Perturbed Free Shear Layers », *Annu. Rev. Fluid Mech.*, vol. 16, nº Volume 16, 1984, p. 365-422, janv. 1984, doi: 10.1146/annurev.fl.16.010184.002053.

[18] O. Marxen, M. Lang, et U. Rist, « Vortex formation and vortex breakup in a laminar separation bubble », *J. Fluid Mech.*, vol. 728, p. 58-90, août 2013, doi: 10.1017/jfm.2013.222.

[19] L. E. Jones, R. D. Sandberg, et N. D. Sandham, « Direct numerical simulations of forced and unforced separation bubbles on an airfoil at incidence », *J. Fluid Mech.*, vol. 602, p. 175-207, mai 2008, doi: 10.1017/S0022112008000864.

[20] J. Moore, D. M. Shaffer, et J. G. Moore, « Reynolds Stresses and Dissipation Mechanisms Downstream of a Turbine Cascade », *J. Turbomach.*, vol. 109, nº 2, p. 258-267, avr. 1987, doi: 10.1115/1.3262096.

[21] C. P. Häggmark, C. Hildings, et D. S. Henningson, « A numerical and experimental study of a transitional separation bubble », *Aerosp. Sci. Technol.*, vol. 5, nº 5, p. 317-328, juill. 2001, doi: 10.1016/S1270-9638(01)01110-5.